

SOFT ROBOTS

An origami-inspired, self-locking robotic arm that can be folded flat

Suk-Jun Kim,^{1,3*} Dae-Young Lee,^{1,2,3*} Gwang-Pil Jung,⁴ Kyu-Jin Cho^{1,2,3†}

A foldable arm is one of the practical applications of folding. It can help mobile robots and unmanned aerial vehicles (UAVs) overcome access issues by allowing them to reach into confined spaces. The origami-inspired design enables a foldable structure to be lightweight, compact, and scalable while maintaining its kinematic behavior. However, the lack of structural stiffness has been a major limitation in the practical use of origami-inspired designs. Resolving this obstacle without losing the inherent advantages of origami is a challenge. We propose a solution by implementing a simple stiffening mechanism that uses an origami principle of perpendicular folding. The simplicity of the stiffening mechanism enables an actuation system to drive shape and stiffness changes with only a single electric motor. Our results show that this design was effective for a foldable arm and allowed a UAV to perform a variety of tasks in a confined space.

INTRODUCTION

Folding is a long-standing and effective solution for space-saving problems in both natural and artificial systems (1–4). A foldable robotic arm is an example of the application of folding in artificial systems, and it can help mobile robots and unmanned aerial vehicles (UAVs) to overcome access issues in difficult environments by allowing them to reach into confined spaces. Foldable or deployable arms can be implemented using various methods including rigid links with conventional joints (5, 6), cylindrical components or bands wrapped around a reel (7–11), and origami-inspired designs (7, 12–14).

Origami-inspired design enables a foldable structure to be lightweight, compact, and scalable while maintaining kinematic behavior because it can replace mechanical components with a pattern of stiff facets and flexure hinges. This unique property makes origami-inspired design widely applied as a method to fabricate robots at various scales and for a variety of applications (13–25). However, the lack of structural stiffness has been a major limitation in the practical use of origami-inspired designs. Ensuring adequate structural stiffness without losing the inherent advantages of simple and lightweight origami structure is a challenging problem. Bistable origami patterns (26, 27), shape memory polymer (SMP) stiffening (25), layer jamming (28, 29), and chemical stiffening methods (7) have been suggested for stiffening mechanism for origami structures.

Providing lightweight and compact actuation for origami structure is another important issue. Actuation of origami-inspired design can be achieved by either direct (generate a torque at each fold line directly) or indirect (apply a force to the entire structure) ways (30). The direct method generally allows the structure to create versatile motions but with high system complexity. In contrast, the indirect method allows the actuation system to be simple but limits a variety of motions. Shape memory alloys (SMAs) (20–24, 30–33) and SMPs or shrinking films (16, 17, 30, 34, 35) have been applied for direct actuation method, and pneumatic force (7, 12) and tendon-driven mechanisms (13–15, 25) have been applied for indirect actuation method.

¹Biorobotics Laboratory, Department of Mechanical and Aerospace Engineering, Seoul National University, Seoul 08826, Korea. ²Institute of Advanced Machines and Design, Seoul National University, Seoul 08826, Korea. ³Soft Robotics Research Center, Seoul National University, Seoul 08826, Korea. ⁴Bio-Inspired Design Laboratory, Department of Mechanical and Automotive Engineering, Seoul National University of Science and Technology, Seoul 01811, Korea.

*These authors contributed equally to this work.

†Corresponding author. Email: kjcho@snu.ac.kr

Copyright © 2018
The Authors, some
rights reserved;
exclusive licensee
American Association
for the Advancement
of Science. No claim
to original U.S.
Government Works

In this study, we suggest an origami-inspired self-locking foldable robotic arm with a tendon-driven actuation system. We used origami-inspired design to achieve a lightweight and a high extension to compression ratio and devised a design method to build a stiffening mechanism that works with multistep folding actuation. Our stiffening mechanism relies on an origami principle of perpendicular folding: Two perpendicular fold lines generate a singularity that constrains each fold line's degrees of freedom. This mechanical locking process can substantially increase the stiffness in the desired direction and is easily reversed because it is a folding process. Restricting the degrees of freedom using orthogonal movements is a widely used method of locking in conventional mechanisms such as door locks. However, unlike the joints with precisely determined movement seen in conventional mechanisms, the joints of origami structures are created by flexible materials and allow undesirable movement. Thus, it is necessary to design the folding pattern while keeping in consideration that the flexibility of the fold line can lead to unexpected problems, such as stiffness reduction.

Actuators usually have a high weight cost, which can be problematic for mobile applications. We implemented a lightweight and compact actuation system that is driven by a single electric motor. This tendon-driven mechanism can actuate both the structure folding and the locking mechanism with a single tendon. The locking mechanism makes the structure easily unlocked by the tendon force while withstanding external forces in the locked mode. Friction was minimized along the tendon path to enhance force transmission and reduce dragging during antagonistic actuation.

The proposed foldable arm is composed of seven foldable modules assembled in series, and we applied the arm to a UAV with an end effector such as a gripper or a camera. The arm allows the UAV to be used to retrieve a target object located within a deep, narrow space and to access locations that are difficult or impossible for a UAV to approach (Fig. 1). The proposed arm weighs 258.6 g, including its actuators. When fully folded and stowed, it is 40 mm in length, and it can be extended up to 700 mm. Testing reveals that a foldable module using the locking mechanism is 5 times more resistant to bending and 200 times more resistant to compression compared with a module without lockers.

RESULTS

Flat foldable arm design with a locking mechanism

The main objective of this study was to design a robotic arm that is foldable to a compact size and has sufficient stiffness. Many researchers

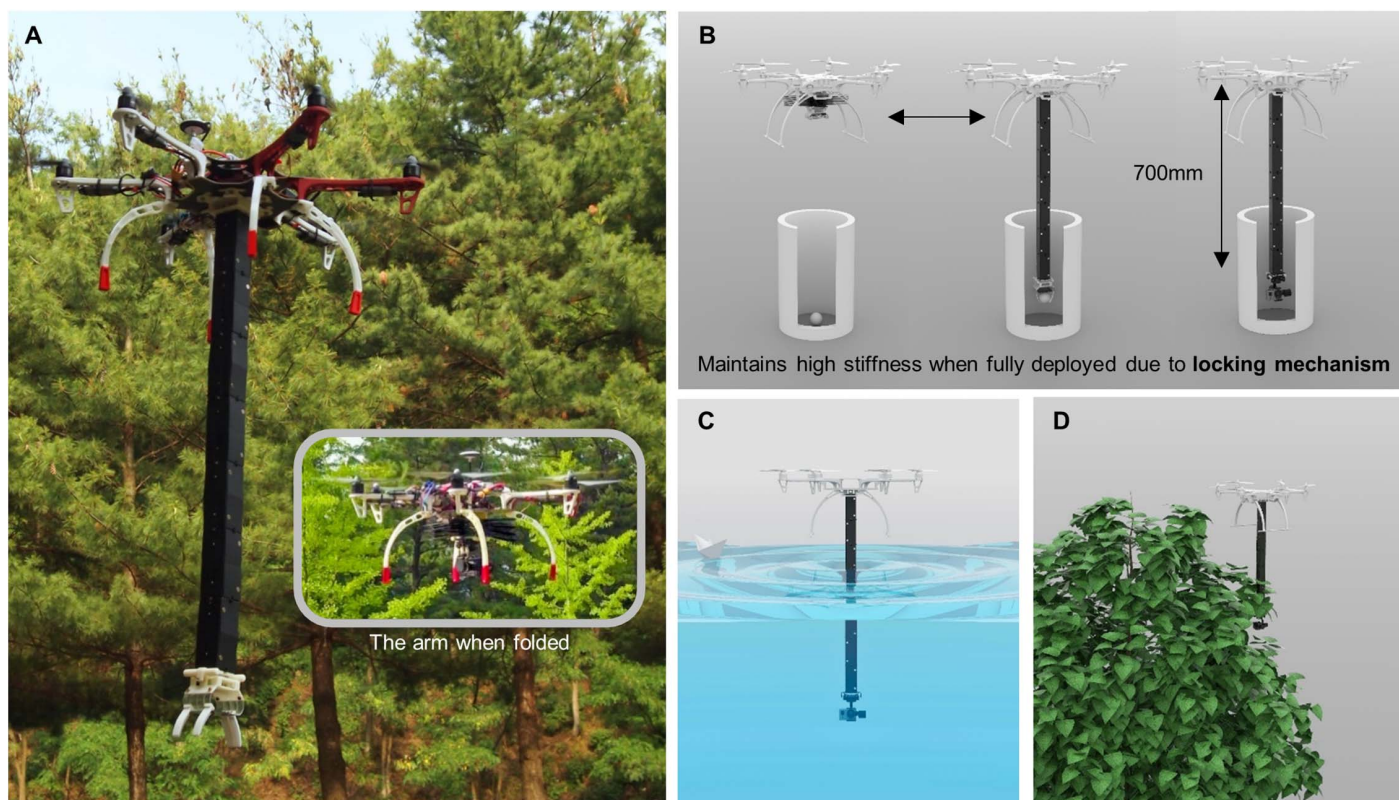


Fig. 1. The foldable robotic arm enabled UAVs to perform tasks that could not be performed otherwise. (A) A UAV equipped with the self-locking foldable robotic arm was tested outdoors. (B) A foldable arm could be folded into a compact volume and deployed on command. The arm equipped with an adequate end effector could grasp an object or inspect inside a narrow, deep space. (C and D) Examples of tasks that could be performed with the foldable arm. The UAV could inspect locations that are difficult to access, such as underwater and spaces between branches. Furthermore, the foldable arm could allow the UAV to obtain samples from crevices in rugged terrain.

have studied flat foldable origami pattern design, and there are several origami design candidates for a foldable arm (12–14, 19, 36–38). Furthermore, not only flat foldability but also sufficient stiffness and a small footprint are required to apply an origami-inspired structure to a robotic arm.

Complex folding patterns are commonly used to create flat, foldable, origami structures that are compact and have a small footprint; however, the structure weakens as the number of fold lines increases. A modular design can be a simple solution to the problem because modules can be stacked to reduce the footprint without substantially increasing the complexity of the structure. In addition, using a modular design makes it easy to expand and modify the whole structure.

In addition, the modular design needed to have reduced degrees of freedom so that the structure could use simple actuation. To achieve this, we used a Sarrus linkage because it generates one degree of freedom in linear motion, which is the simplest possible closed linkage chain, to the best of our knowledge. The Sarrus linkage in this study consisted of a top square, a bottom square, and four chains. Each chain was connected to each side of the square and consisted of two links and three joints. The lengths of each link were identical, which allowed the structure to be flat and foldable (Fig. 2, A to C).

Foldable structures can be deformed undesirably by external forces—meaning that a structure’s stiffness must be high enough to meet the requirements associated with different tasks; it should or should not be folded to suit the needs of different situations. For this application,

the arm should be rigid in its deployed state but not in its folded state. In addition, configuration of the fold line is another important design factor. Most origami-inspired foldable structures use flexible materials to generate fold lines. The widths of the fold lines are generally determined by the thickness of the facet material. When the fold line width is excessive, the rigidity of the entire structure is greatly weakened. It is then essential to minimize fold line width when the structure needs to have high rigidity.

Implementation of a stiffening mechanism was done by adjusting the shape of the Sarrus linkage and adding an extra facet called a locker (fig. S8). The locker had no fold lines along the stiffening direction and was wedged inside the structure to restrict the mobility of the Sarrus linkage (Fig. 2E). In its locked mode, the module was fully deployed and the lockers were locked in place until the lockers made contact with the U1-B1 facet (Fig. 2D). To prevent the module from folding, the lockers were wedged between the top and bottom plates in the locked position. Decoupling mode change from the occurrence of external forces is also a necessary consideration due to an external force’s potential to compromise the structural stability of the module. We decoupled these two conditions by applying the principle of perpendicular folding—if two fold lines are perpendicular, they generate a singularity that decouples their ability to simultaneously fold because only one fold line can be folded along at a time; this mode change only occurs when all facets are in the same plane. From Fig. 2, this concept is applied to the fold line of the locker joint (m) and its perpendicular

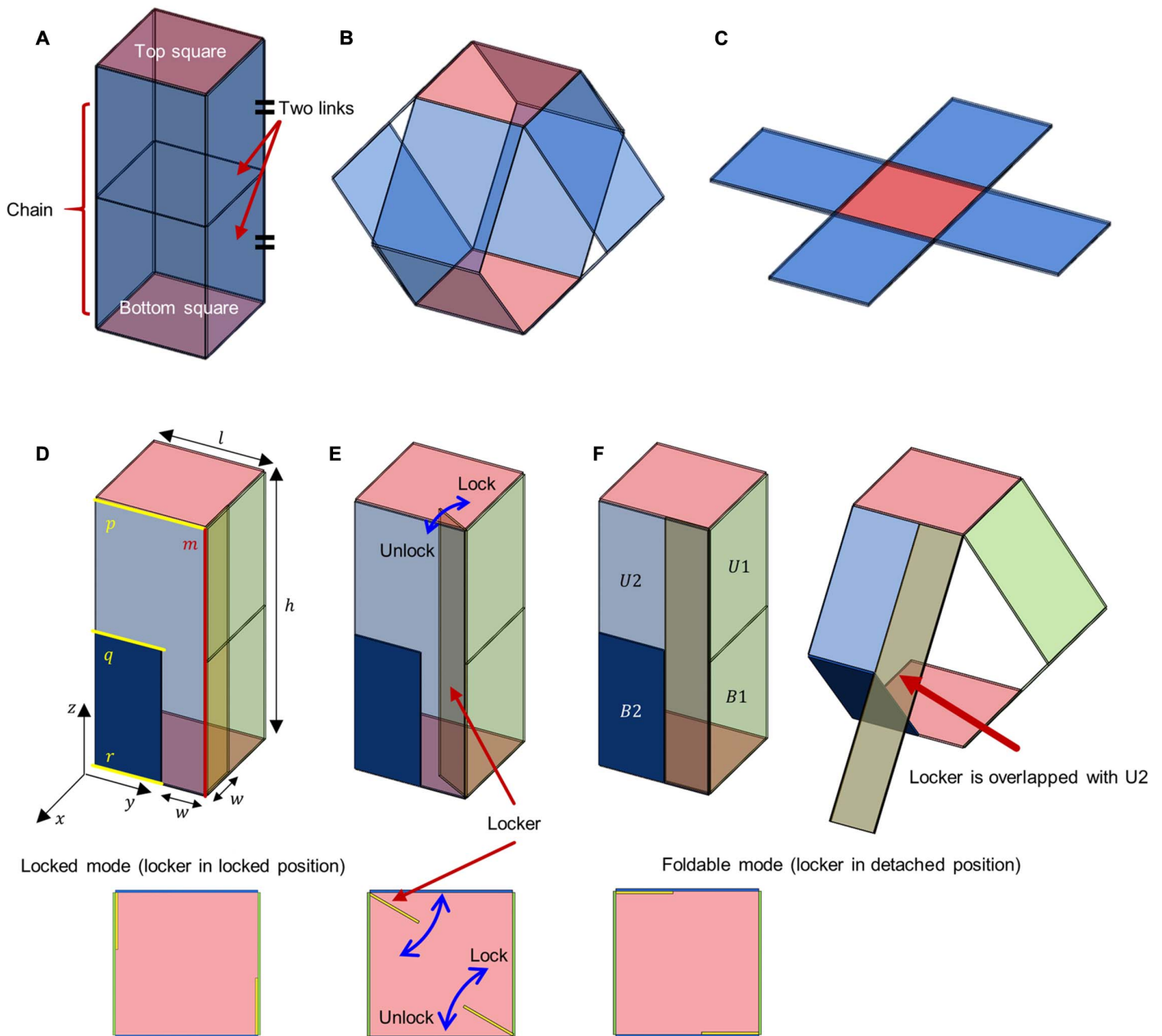


Fig. 2. Foldable module with locking mechanism. (A to C) Foldable structure using Sarrus linkage. (D to F) Locking mechanism by adjusting the shape of the Sarrus linkage and adding an extra facet. (A) Deployed state. The Sarrus linkage with four chains assumes a square column shape when deployed. (B) Transition state. (C) Folded state. The Sarrus linkage can be folded flat when the two links are of the same length. (D) In the locked mode, the fold line p to r cannot be folded because the lockers are in the locked position. The locking mechanism constrained the degrees of freedom of the foldable module and increased its stiffness. (E) Locker in the transitional position. (F) In the foldable mode, the lockers are in the unlocked position. The lockers were unlocked from the U1-B1 facet and overlapped with U2. Because all facets were in the same plane, the fold line p to r could be folded. Upper figures depict trimetric views of the module. The figure shows only the frontal two chains for simplicity. Lower figures depict a top view of the module.

counterpart joints (p - r) that constitute the Sarrus linkage. Therefore, the force required to rotate the lockers was perpendicular to the force required to fold the module. In contrast, when the module was in its foldable mode, the lockers are unlocked from the U1-B1 facet and were overlapped with U2 as shown in Fig. 2F.

The foldable module has three variables: l , length of one side of the top and bottom square; h , height of the module; and w , width of the

locker. In the fabricated modules, l , h , and w were 40, 100, and 16 mm, respectively. A single module weighed 27.5 g and could withstand compressive forces over 15 kg-f. The modules were fabricated by a multimaterial planar fabrication method (15), which used a large difference in stiffness between the facet and fold line materials and enabled easy construction of the linkage structure. Details of the fabrication method are provided in Materials and Methods.

Design of the actuation system driven by a single electric motor

To ensure the lightweight advantage of the modular structure, which is a highly desirable attribute for mobile applications, we aimed to design an actuation system that uses the minimum number of actuators while also being reliable and repeatable. Various low-profile smart materials such as SMAs and electroactive polymers have been used to successfully actuate origami structures by directly applying a torque to fold lines (30). These direct actuation methods provide high degrees of freedom, but their reliability and robustness are not superb. Pneumatic actuation has been used with origami structures, and it is an effective method for transmitting force from a single actuation source to a whole body (12). However, it requires an air pump, which is usually heavier than an electric motor. In this study, we propose a tendon-driven actuation system with a single electric motor, which can be lightweight and can be applied to scalable structures.

Folding is used in two ways in the proposed arm: for structure folding and for the locking mechanism. These two different folding processes should be driven sequentially, and they require forces that are perpendicular to each step. Because tendon-driven actuation with a single electric motor normally provides actuation with one degree of freedom, driving two folding steps with a single tendon is a challenging problem. Structure folding of serially assembled Sarrus linkages allows a single tendon to change the overall structure with high scalability—the number of modules does not affect the complexity of actuation. However, the locking mechanism requires additional actuation. To use a single tendon to exert force in two different directions, we need to distort the tendon path for each locker, which induces tendon friction

and lowers the force transmission efficiency. Thus, to solve this problem, we designed a variable tendon path consisting of a curved slit path on the lockers. The slit design made it possible to exert a large force for the locking mechanism but also allowed the tendon to move along the slit to reduce path distortion during the structural change.

Details of the actuation mechanism are shown in Fig. 3. Figure 3A describes a module with two adjoining chains at the n th layer from the top. The tendon path consisted of two holes and one slit. Two holes, A_n and O_n , were located on the top and bottom squares, respectively, and a slit connecting points B_n and C_n was located on the lockers. To facilitate tendon connection between modules, we placed A_n and O_n on the top and bottom squares, and these points were assumed to be located at the center of each side. We designed the tendon to enter the module through hole A_n from the $(n - 1)$ th layer, pass through the slit on a locker, and come out through hole O_n to the $(n + 1)$ th layer, as shown in Fig. 3. When the lockers were in the locked position, two kinds of forces were applied to the module by pulling the tendon from upside (regarding the top square as fixed and O_n as the end of the tendon). A force (F_L) drove the lockers to rotate around the joint and to be unlocked from the U1-B1 facet, and a compressive force parallel to the z axis (F_Z) drove the module into the folded state. Because lockers constrained the module's degrees of freedom and withstood F_Z , the module could not be folded and only the lockers could be rotated. When the lockers were unlocked and overlapped with U2, the module regained its degrees of freedom and could be folded by the tension, enabling sequential folding by a single tendon. In the case of deploying the module, a tensile force in the z -axis direction was required. A flexible tendon cannot push the module or the lockers by unwinding the pulley, so

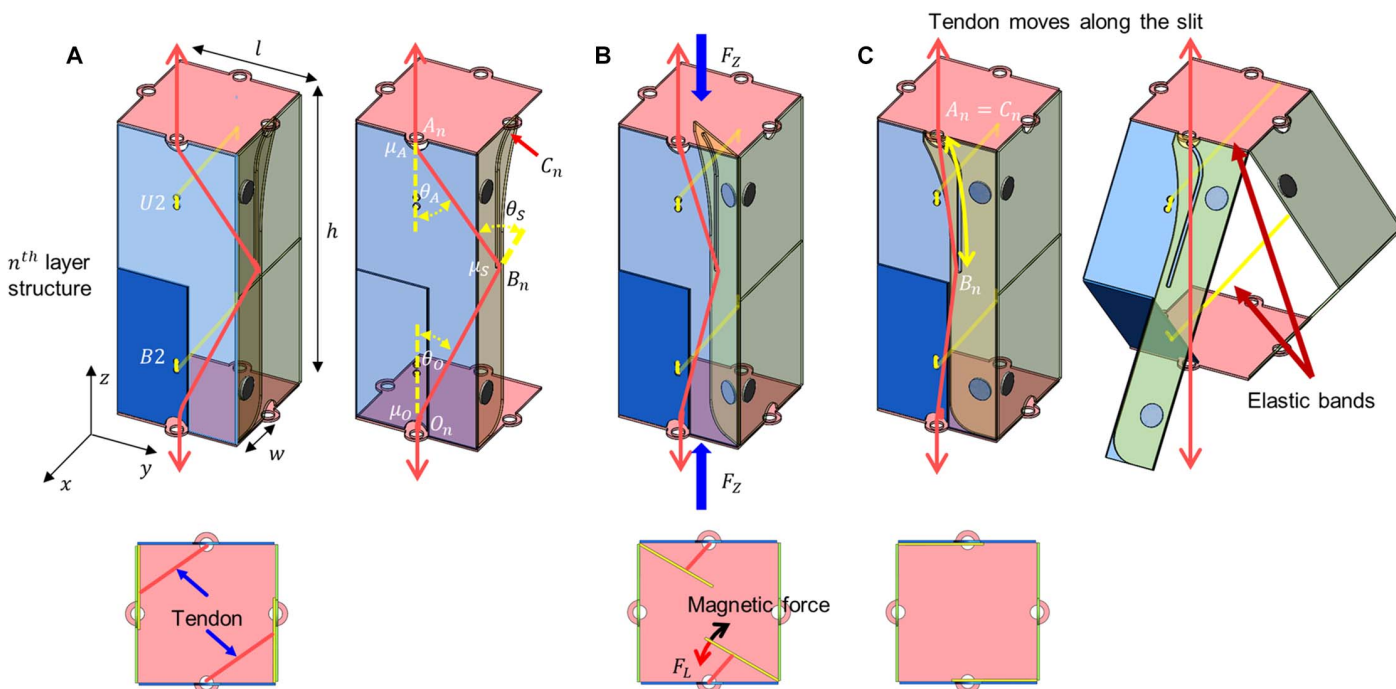


Fig. 3. Tendon path design of the module. Tendon friction was minimized to increase force transmission and not to constrain antagonistic actuation. The folding process is in order of A to C. The deployment process follows the reverse order. (A) Tendon path when the module is deployed and the lockers are locked. (B) Locker in transitional position. When the tendon was pulled upward to fold the module, F_Z and F_L were applied to the module. (C) Tendon path when the module is being folded. During folding, the tendon moved along the slit from B_n to C_n (yellow double-headed arrow). During deployment, the tendon stayed at C_n owing to the bent slit. Upper figures depict trimetric views of the module. The figure shows only two frontal chains for simplicity. Lower figures depict a top view of the module.

elastic rubber bands and magnets were used for antagonistic actuation. The elastic bands were installed between chains that are facing each other (Fig. 3C), and the magnets were installed on the lockers and adjoining U1-B1 facets (fig. S8). When the tendon was unwound, the module was

deployed via the elastic force of the rubber bands and the force of gravity, and when the module was fully deployed, the lockers were passively rotated and locked by magnetic force. A detailed explanation on how to route the tendon path design to reduce friction is presented in the Supplementary Text.

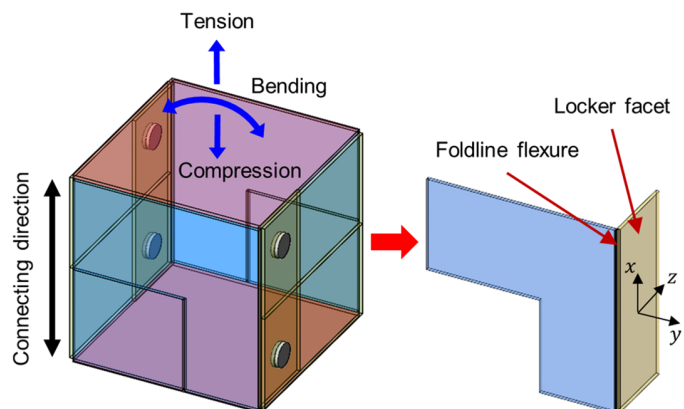


Fig. 4. Types and directions of external forces on the module and coordination representing the movement of the locker. In the performance study, we analyzed the mechanical responses of the module according to the change of the design parameters in the compression direction and the bending direction shown in the figure. Because the relative motion of the lockers is an important factor in determining the mechanical response, a coordinate system shown in the figure is used to describe the motion of the lockers.

Performance study on the module design

Stiffening via folding is a key feature of this paper. Therefore, mechanical properties, such as the stiffness and the maximum load capacity, would be a crucial standard for the evaluation of the mechanism’s structural performance. However, it is difficult to use analytical methods to investigate the effects of the module’s geometric design parameters on mechanical properties, owing to complex material composition and geometry. Rather, this study used empirical methods to investigate the relationship between the design parameters and the mechanical properties of the structure.

A cube-shaped module with a side length of 40 mm and a locker width of 8 mm was selected as a reference, and the experiments were carried out by changing specific design parameters, whereas the others were fixed as reference values to see how they would affect the mechanical properties of the structure. Normalized design parameters were defined as follows: \hat{l} , normalized side length; \hat{h} , normalized height; \hat{w} , normalized locker width. \hat{l} and \hat{h} were normalized by the side length of the reference module, 40 mm, and \hat{w} was normalized by \hat{l} , the length of one side of the top and bottom square, to identify the scale effect of \hat{l} when maintaining the ratio of the locker. Performance tests were

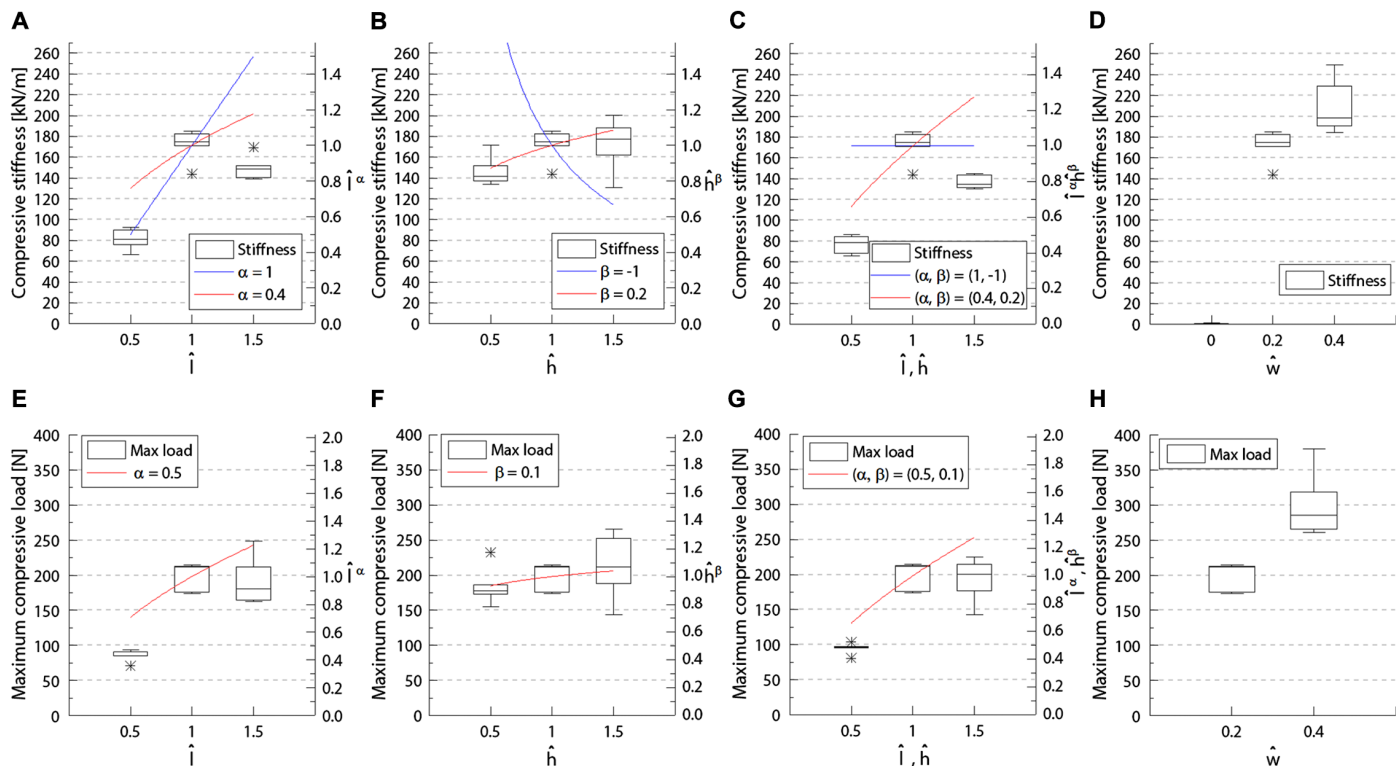


Fig. 5. Results of the performance study experiment: Compression (sample size: $n = 5$). (A) Compressive stiffness of the module when \hat{l} was changed. (B) Compressive stiffness of the module when \hat{h} was changed. (C) Compressive stiffness of the module when \hat{l} and \hat{h} were both changed. (D) Compressive stiffness of the module when \hat{w} was changed. (E) Maximum compressive load when \hat{l} was changed. (F) Maximum compressive load when \hat{h} was changed. (G) Maximum compressive load when \hat{l} and \hat{h} were both changed. (H) Maximum compressive load when \hat{w} was changed. Blue plots on the figures represent bending stiffness trend according to the general beam theory. Red plots on the figures represent the trend of results that are driven by least-squares methods. α and β are exponents of \hat{l} and \hat{h} , respectively. Whiskers are extended to 1.5 times of interquartile range (IQR) from the edge of the box; IQR is difference between upper and lower quartile. Asterisks indicate outliers that are beyond the whiskers.

performed to examine the stiffness and the maximum load capacity under compression and bending load. Because the mechanical properties from tensile loading were determined by material performance rather than structural characteristics, we excluded tensile testing from the analysis. The material properties of the fold line material are attached to the Supplementary Materials.

The module response to compressive loading is shown in Fig. 5. The expected trend curve from conventional solid mechanics and the actual trend curve estimated with the least-squares method are indicated by blue and red lines, respectively. According to the general beam theory, compressive load resistance is proportional to \hat{l} and inversely proportional to \hat{h} . However, Fig. 5A indicates that the change in compressive stiffness gradually decreased as \hat{l} increased. Figure 5B rather indicates a reverse trend compared with the expected results. As the normalized height, \hat{h} , increased, the compressive stiffness increased. These trends can also be seen in Fig. 5C, where the stiffness increased when both \hat{l} and \hat{h} changed simultaneously. For the locker width, the change in compressive stiffness gradually decreased as \hat{w} increased, as shown in Fig. 5D. We presumed that this is because the stiffness is mainly determined by undesirable rotation of the facets caused by flexibility of the fold lines, not the deformation of the facets.

When compression was exerted on the structure, the locker rotated in the y and z directions, as indicated in Fig. 4. The shape of the locker was an important factor in determining the angle of rotation. When the locker width was too small, it rotated in both the y and z directions ($\hat{l} = 0.5$ in Fig. 5A). When w was widened as \hat{l} increased, the stiffness

rapidly increased because a locker with large width can prevent rotation in the y direction. However, the increase in stiffness rapidly declined, because the increase of w did not prevent the rotation in the z direction. In the case of \hat{h} , the locker got longer in the fold line direction when \hat{h} increased. This elongated shape caused the locker to rotate less within the same fold line width, strengthening the structural stiffness.

The maximum load was measured at the moment when the module failed. This occurred most frequently when the locker popped out of the module. Locker popping was difficult to quantify but could be described by behavior similar to the locker's stiffness analysis. When the locker width was short, the locker had a high possibility to pop out because the locker rotated in the y and z directions. Therefore, a wider locker was preferred to withstand high compression loading. Similar to the stiffness case, the rate of increasing the stiffness rapidly declined as the locker width increased over a certain length. The general response to maximum compressive loading showed similar aspects with the results of compressive stiffness, as shown in Fig. 5 (E to H).

Figure 6 presents the response of the module against the bending load. The module had anisotropic bending properties because of the position of the locker. When the plane direction of the locker was parallel to the bending direction, the force induced the locker to rotate in the y direction; when it was perpendicular, the force induced the locker to rotate in the z direction. The locker was expected to be more susceptible to rotation in the z direction; therefore, bending stiffness and the maximum load were investigated in perpendicular direction.

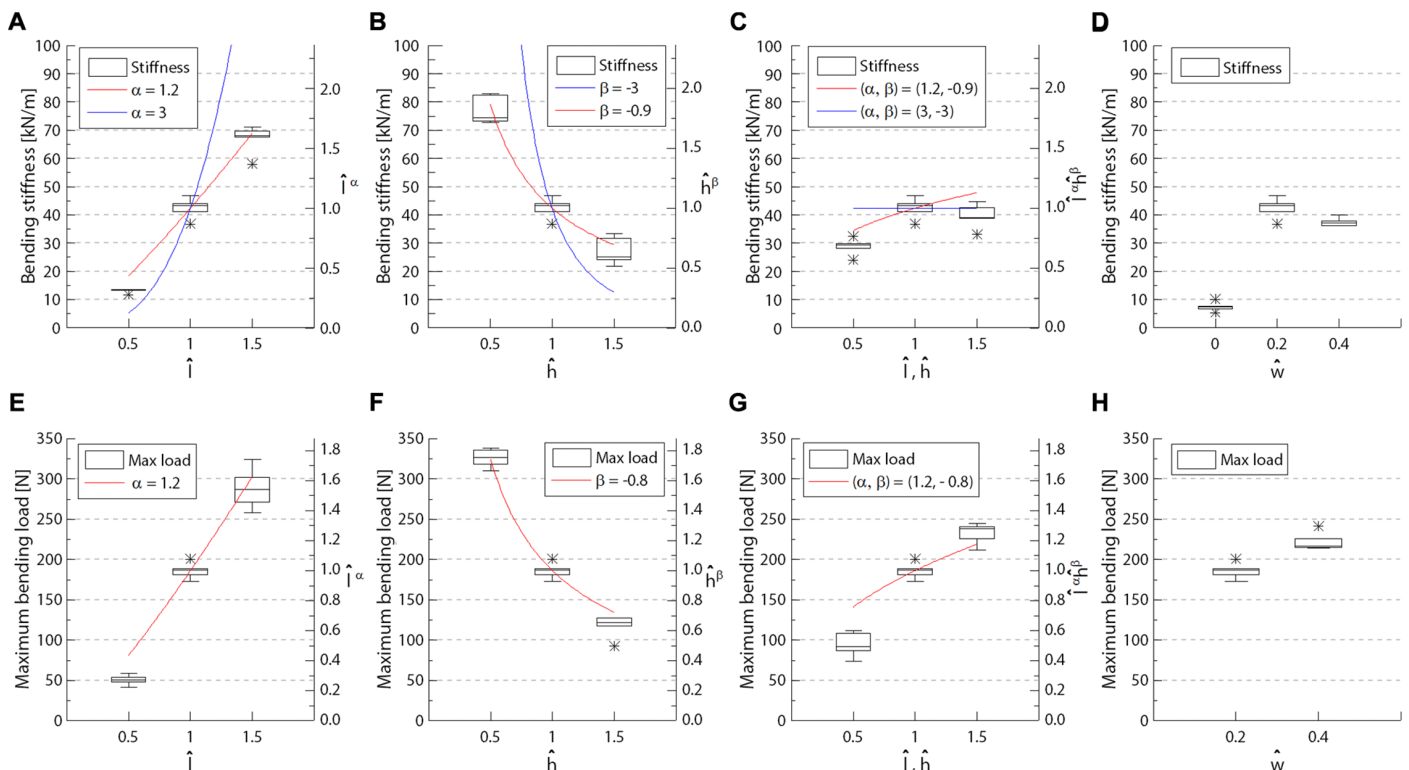


Fig. 6. Results of the performance study experiment: Bending (sample size: $n = 5$). (A) Bending stiffness of the module when \hat{l} was changed. (B) Bending stiffness of the module when \hat{h} was changed. (C) Bending stiffness of the module when \hat{l} and \hat{h} were both changed. (D) Bending stiffness of the module when \hat{w} was changed. (E) Maximum bending load when \hat{l} was changed. (F) Maximum bending load when \hat{h} was changed. (G) Maximum bending load when \hat{l} and \hat{h} were both changed. (H) Maximum bending load when \hat{w} was changed. Blue lines on the figures represent expected bending stiffness trend according to the general beam theory. Red lines on the figures represent the trend of results that are driven by least-squares methods. α and β are exponents of \hat{l} and \hat{h} , respectively. Whiskers are extended to 1.5 times of IQR from the edge of the box; IQR is difference between upper and lower quartile. Asterisks indicate outliers that are beyond the whiskers.

According to the general beam theory, the bending stiffness should be proportional to the cube of \hat{l} and inversely proportional to the cube of \hat{h} . The actual trend was different, similar to the response by the compressive load. In Fig. 6A, the bending stiffness increased as \hat{l} got longer, because the Sarrus linkage has zero degrees of freedom in the bending direction, but not as high as expected due to stiffness loss caused by locker rotation. In the case of \hat{h} in Fig. 6B, the structure showed much higher stiffness than expected. It can be inferred that the stiffness increased as the rotation of the locker was reduced because the locker's length in fold line direction became longer.

The maximum bending load appeared to be determined by how much the locker rotates, similar to the compressive response. The experimental results show that the stiffness and the maximum load tended

to be similar to the bending response shown in Fig. 6 (E to H). For a particular length requirement for the foldable arm, it is advantageous to reduce the total number of modules and instead increase the length of individual modules.

As a result of the design parameter studies, it was confirmed that a large \hat{h} improved performance, but \hat{l} did not improve performance as expected, considering volume and weight increases. \hat{w} improved performance drastically up to a certain length but did not show a substantial performance improvement with further increase. From this, module parameters were determined most effective when l , h , and w were 40, 100, and 16 mm, respectively for this application. A detailed report of the results from the performance experiment is included in the Supplementary Materials.



Fig. 7. The foldable robotic arm with seven modules assembled in series. (A) Stills from a movie that shows folding process of the arm. **(B)** Foldable arm picking up objects with its gripper at the bottom of a 500-mm-deep ditch. **(C)** A camera and a gimbal were attached to the arm and filmed between branches.

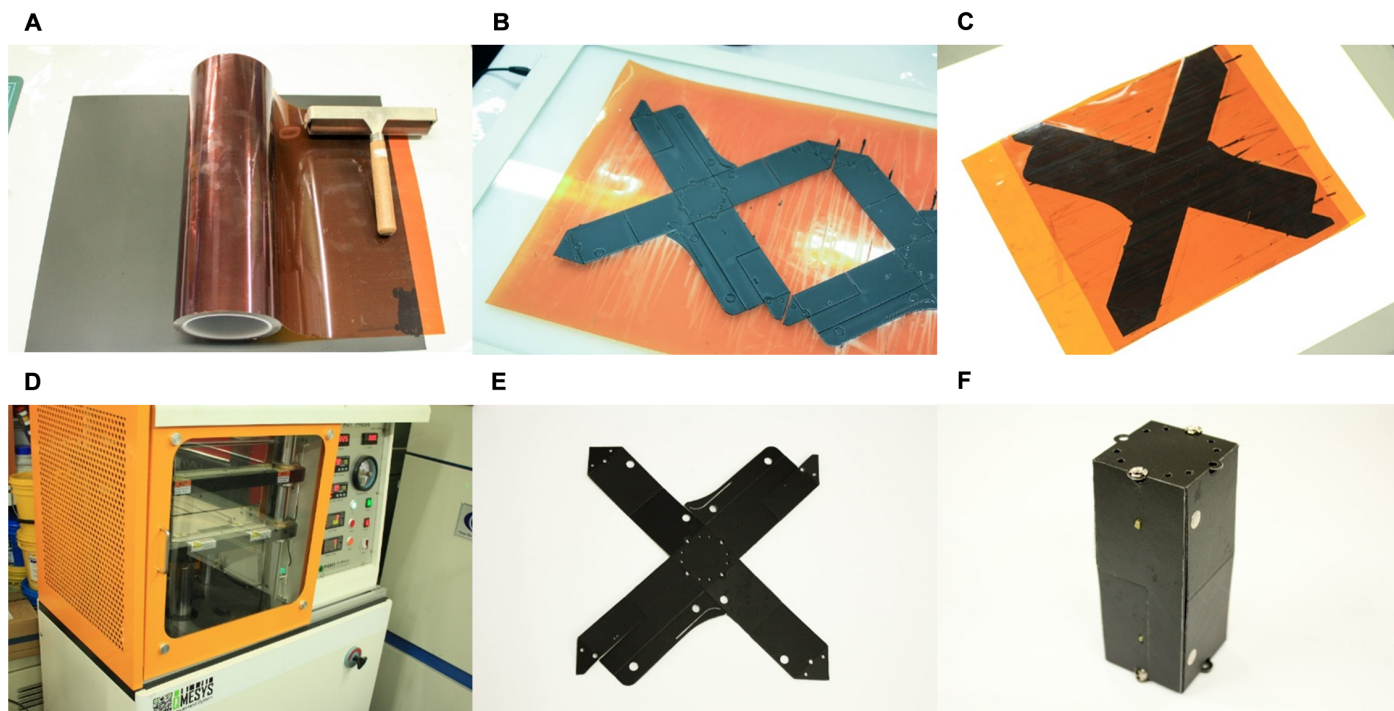


Fig. 8. Steps in the fabrication process of the foldable module.

The foldable arm in application

The foldable arm was validated through indoor and outdoor tests. In the indoor test, the arm was deployed and folded repeatedly, and various objects were gripped with the buckling gripper (fig. S10 and movie S5; see Supplementary Text) (39). The buckling gripper was redesigned to be fully foldable and provided many contacts with even contact forces, which enabled adaptive gripping. As shown in Fig. 7A, the 700-mm arm was able to fold itself to a 40-mm height, achieving an extension-to-compression ratio of 17.5:1. The stills in Fig. 7A were captured at intervals of 8 s. It took 40 s for the arm to fully fold itself (movie S3).

In the outdoor test, first, the UAV carried the folded arm over a ditch, and the arm fully deployed itself. The UAV then lowered itself enough to allow the gripper to pick up an object at the bottom of the ditch without entering the ditch itself (Fig. 7B and movie S4). The ditch was narrow enough to pose a danger to the UAV: The ditch was 600 mm wide, and the UAV's diameter was 550 mm. The arm successfully folded itself and stowed itself away in the landing gear during takeoff and landing. Second, the arm was equipped with a gimbal (3DIII metal gimbal TL3T01, Tarot) and a GoPro camera (GoPro Hero 3+, GoPro) to perform videotaping near trees and among tree branches, as shown in Fig. 7C and movie S4. The UAV used for outdoor tests of the foldable arm was the DJI F550 frame kit (F550 ARF KIT, DJI).

DISCUSSION

In this study, we designed an origami-inspired self-locking foldable robotic arm with tendon-driven actuation system. Using the origami-inspired design allowed us to develop lightweight modules that are 100 mm in height and weighs 27.5 g. We also implemented a self-locking mechanism using the principle of perpendicular folding. We measured the maximum bending load and bending stiffness of the

module and determined that modules with lockers are about 5 times stiffer against bending and 200 times stiffer against compression than those without lockers. We used seven modules to assemble the foldable arm and attached a UAV to one end of the arm and a gripper or a gimbal and a camera to the other. The resulting assembly was validated and performed a variety of tasks.

The foldable arm endows UAVs with the ability to perform tasks in areas too small for a UAV to enter. For example, equipping the arm with a gimbal and a camera would enable a UAV to inspect small chimneys and narrow-bore pipes. The foldable arm can also allow UAVs to perform tasks in areas where the terrain makes a safe landing impossible, such as obtaining samples from crevices in rugged terrain. Future work could design a foldable arm that extends from the top of a UAV, which would enable such tasks as performing a visual inspection beneath a bridge and perching on a structure to save energy. Mobile robots could use the foldable arm to perform tasks while exploring confined spaces, taking advantage of the foldable arm's compact storage volume.

The arm in this study has several limitations that need to be overcome in future work. First is the length of the arm. Fabricating the arm longer by stacking more modules together also increased tendon friction, which hindered its antagonistic actuation and prevented the arm from operating properly. Module height could be increased to overcome this problem, but doing so would increase the foldable arm's footprint. It is impossible to completely eliminate tendon friction, but an active locking mechanism with extra actuation could be used to eliminate distortion of the tendon path and to accommodate increases in the arm length. A second limitation is the stiffness of the arm. Structural stiffness modeling is needed to find optimized variable sets, and the weak intermodular assembly should be enhanced. The adhesives and eyelets used to connect the modules did not guarantee firm mechanical bonding between modules (figs. S1 to S3). The weakness of the intermodular assembly made the deployed arm unstable when

the UAV flew fast. One possible solution is to fabricate the foldable arm as a body instead of separate units, or a method for interlocking the modules could be devised. The final limitation is the arm's limited degrees of freedom. Although UAVs have six degrees of freedom, the foldable arm in this study could only pick up objects from a limited range of directions because it has no joints. To enable complex tasks, the arm needs to have more degrees of freedom. In future work, modules with low-profile origami joints that are compact and lightweight could be designed.

MATERIALS AND METHODS

Fabrication

To fabricate the foldable module, we used a multimaterial planar fabrication method (15) that was developed to build origami structures by giving stiffness difference between facets and fold lines. Polyethylene terephthalate (PET) film with thermal adhesive on one side (0.35 mm; ARO Tech) was chosen for the facets, and the ripstop fabric (0.2 mm; ARO Tech) was chosen as a compliant material for the fold lines. The following steps describe the process:

1) Sticky polyamide film (CT-1065, Coretec) was attached to the side of the PET film with no thermal adhesive (Fig. 8A).

2) Desired patterns were laser-cut (VLS 3.5, Universal Laser System) from two PET films and the ripstop, and excess material was removed (Fig. 8B).

3) The cut ripstop pattern was sandwiched between patterns cut from the PET films. Backlighting was used to align the patterns (Fig. 8C).

4) The sandwiched structure was pressed in an automated heat presser (QM900A, QME-SYS) for 5 min at 110°C and 0.5 MPa to melt the thermal adhesive so that the PET films and the ripstop could be bonded together (Fig. 8D).

5) After 10 min of cooling at room temperature below a steel plate and a 2-kg weight, the polyamide film was peeled off, and the ripstop fabric that protruded from the structure was removed (Fig. 8E).

6) Neodymium magnets were installed with tapes, and elastic rubber bands were installed. The module was assembled with two-sided tape and eyelets. The final model is shown in Fig. 8F. l , h , and w of the model are 40, 100, and 16 mm, respectively.

Most of the other structural parts were fabricated with a three-dimensional printer (uPrint SE Plus, Stratasys).

By assembling seven modules, the proposed arm was able to reach up to 700 mm below the UAV and weighed 258.6 g, including actuation system. Detailed specifications of the prototype are written in table S2. In addition, a connector that assembles the arm and end effector was designed to allow the gripper to be easily changed out for the gimbal with attached GoPro camera. Spur-gear motors with encoders were chosen for actuating the arm and the gripper [RA-12WGM 02TYPE (6V) with 2channel Encoder, 298:1; D&J WITH Co. Ltd.]. Arduino Micro and XBee S1 modules were chosen as the microcontroller and wireless communication device used to control the arm and the gripper.

Experiments

For the performance study experiment, we fabricated samples by changing l , h , and w to analyze the independent effects of variables on model stiffness. As shown in fig. S11, four sets of samples were prepared: (i) by changing l from 20 to 60 mm in 20-mm increments while keeping w at 20% of l and h at 40 mm, (ii) by changing h from 20 to 60 mm in 20-mm increments while keeping w at 20% of l and l

at 40 mm, (iii) by changing both l and h from 20 to 60 mm in 20-mm increments simultaneously while keeping w at 20% of l , and (iv) by changing w from 0 to 40% of l in 20% increments while keeping l and h at 40 mm. The sizes of magnets were chosen to be proportional to l . For each l from 20 to 40 to 60 mm, the diameter of the magnets changed from 3 to 5 to 8 mm. The design of every sample fabricated for experiments was simplified; lockers were simplified to rectangular shape, and tendon paths were removed. However, in the case of samples for robustness experiment in the Supplementary Materials, samples were fabricated just the same as the one used for the foldable arm.

For the bending test, we installed 4T acrylic plate inside and outside of the samples at both ends of the module, and fixed end was bolted to an aluminum test bed as shown in fig. S6A. Shear force was exerted at the free end of the module. The length of one side of acrylic plate that was installed inside the module was set at 90% of l . For the compression test, the bottom square of the module was bolted to the test bed, and the compressive force was exerted to the module as shown in fig. S6B. For each sample, the stiffness of the module and maximum load that the module could withstand were measured, and all experimental results were measured with a universal testing machine (model RB302, R&B) and a load cell (model UMM-K100, Dacell).

Because the module stiffness is highly nonlinear, linear approximation was conducted to calculate the stiffness. We drew tangent lines throughout the force-displacement graphs and chose the steepest slope as the module stiffness. The displacement interval for calculating the slope was 1 mm. In the case of measuring the maximum load, we chose the maximum force value on the force-displacement graphs. Results are depicted using a box plot format and Tukey-style whiskers.

SUPPLEMENTARY MATERIALS

robotics.sciencemag.org/cgi/content/full/3/16/earr2915/DC1

Text

Fig. S1. Results of performance experiment: Bending (sample size: $N = 5$).

Fig. S2. Results of performance experiment: Compression (sample size: $N = 5$).

Fig. S3. Results of performance experiment: Tensile stiffness (sample size: $N = 5$).

Fig. S4. Results of performance experiment: Robustness (sample size: $N = 3$).

Fig. S5. Force-displacement graph under compressive and bending loads.

Fig. S6. Experimental setup.

Fig. S7. Experimental setup for repeatedly folding the module.

Fig. S8. Origami-inspired pattern design of the foldable module.

Fig. S9. Schematics of the foldable module for tendon friction modeling.

Fig. S10. The lightweight and compact buckling gripper.

Fig. S11. Fabricated samples with different variable sets.

Table S1. Variables for the foldable module assuming [l, h, w] = [40, 100, 16] (mm).

Table S2. Specifications for the foldable arm.

Table S3. Tensile test results of ripstop fabric.

Table S4. Parameters chosen for the buckling gripper.

Table S5. Experimental results of performance study experiment: Compression.

Table S6. Experimental results of performance study experiment: Bending.

Table S7. Experimental results of application performance experiment.

Movie S1. Tendon-driven foldable module.

Movie S2. Foldable module with locking mechanism.

Movie S3. Foldable arm indoor test.

Movie S4. Foldable arm outdoor test.

Movie S5. Lightweight and compact buckling gripper.

Reference (40)

REFERENCES AND NOTES

1. D. S. A. De Focatiis, S. D. Guest, Deployable membranes designed from folding tree leaves. *Philos. Trans. A Math. Phys. Eng. Sci.* **360**, 227–238 (2002).
2. J. F. V. Vincent, Deployable structures in nature: Potential for biomimicking. *Proc. Inst. Mech. Eng. C* **214**, 1–10 (2000).

3. B. Kresling, Coupled mechanisms in biological deployable structures, in *IUTAM-IASS Symposium on Deployable Structures: Theory and Applications* (Springer, 2000), pp. 229–238.
4. E. Morris, D. A. McAdams, R. Malak, The state of the art of origami-inspired products: A review, *Proceedings of the ASME 2016 International Design Engineering Technical Conferences and Computers and Information in Engineering Conference*, Charlotte, NC, 21 to 24 August 2016 (ASME, 2016).
5. C. M. Korpela, T. W. Danko, P. Y. Oh, MM-UAV: Mobile manipulating unmanned aerial vehicle. *J. Intell. Robot. Syst.* **65**, 93–101 (2012).
6. V. A. Sujan, S. Dubowsky, Design of a lightweight hyper-redundant deployable binary manipulator. *J. Mech. Des.* **126**, 29–39 (2004).
7. M. Schenk, A. D. Viquerat, K. A. Seffen, S. D. Guest, Review of inflatable booms for deployable space structures: Packing and rigidization. *J. Spacecr. Rockets* **51**, 762–778 (2014).
8. J. Block, M. Straubel, M. Wiedemann, Ultralight deployable booms for solar sails and other large gossamer structures in space. *Acta Astronaut.* **68**, 984–992 (2011).
9. E. W. Hawkes, L. H. Blumenschein, J. D. Greer, A. M. Okamura, A soft robot that navigates its environment through growth. *Sci. Robot.* **2**, eaan3028 (2017).
10. T. Kuciński, T. Rybus, K. Seweryn, M. Banaszekiewicz, T. Buratowski, G. Chmaj, J. Grygorczuk, T. Uhl, Deployable manipulator technology with application for UAVs, in *Aerospace Robotics II* (Springer, 2015), pp. 93–103.
11. F. Collins, M. Yim, Design of a spherical robot arm with the spiral zipper prismatic joint, *Proceedings of the 2016 IEEE International Conference on Robotics and Automation (ICRA)*, Stockholm, Sweden, 16 to 21 May 2016 (IEEE, 2016).
12. R. V. Martinez, C. R. Fish, X. Chen, G. M. Whitesides, Elastomeric origami: Programmable paper-elastomer composites as pneumatic actuators. *Adv. Funct. Mater.* **22**, 1376–1384 (2012).
13. K. Zhang, C. Qiu, J. S. Dai, An extensible continuum robot with integrated origami parallel modules. *J. Mech. Robot.* **8**, 031010 (2016).
14. T. Liu, Y. Wang, K. Lee, Three-dimensional printable origami twisted tower: Design, fabrication, and robot embodiment. *IEEE Robot. Autom. Lett.* **3**, 116–123 (2017).
15. D.-Y. Lee, S.-R. Kim, J.-S. Kim, J.-J. Park, K.-J. Cho, Origami wheel transformer: A variable-diameter wheel drive robot using an origami structure. *Soft Robot.* **4**, 163–180 (2017).
16. S. Felton, M. Tolley, E. Demaine, D. Rus, R. Wood, A method for building self-folding machines. *Science* **345**, 644–646 (2014).
17. S. Miyashita, S. Guitron, S. Li, D. Rus, Robotic metamorphosis by origami exoskeletons. *Sci. Robot.* **2**, eaao4369 (2017).
18. G.-P. Jung, K.-J. Cho, Frog-hopper-inspired direction-changing concept for miniature jumping robots. *Bioinspir. Biomim.* **11**, 056015 (2016).
19. C. D. Onal, R. J. Wood, D. Rus, An origami-inspired approach to worm robots. *IEEE/ASME Trans. Mechatron.* **18**, 430–438 (2013).
20. M. Noh, S.-W. Kim, S. An, J.-S. Koh, K.-J. Cho, Flea-inspired catapult mechanism for miniature jumping robots. *IEEE Trans. Robot.* **28**, 1007–1018 (2012).
21. A. Firouzeh, J. Paik, Robogami: A fully integrated low-profile robotic origami. *J. Mech. Robot.* **7**, 021009 (2015).
22. J.-S. Koh, E. Yang, G.-P. Jung, S.-P. Jung, J. H. Son, S.-I. Lee, P. G. Jablonski, R. J. Wood, H.-Y. Kim, K.-J. Cho, Jumping on water: Surface tension-dominated jumping of water striders and robotic insects. *Science* **349**, 517–521 (2015).
23. J.-S. Koh, K.-J. Cho, Omega-shaped inchworm-inspired crawling robot with large-index-and-pitch (LIP) SMA spring actuators. *IEEE/ASME Trans. Mechatron.* **18**, 419–429 (2013).
24. M. Boyvat, J.-S. Koh, R. J. Wood, Addressable wireless actuation for multijoint folding robots and devices. *Sci. Robot.* **2**, eaan1544 (2017).
25. A. Firouzeh, J. Paik, An under-actuated origami gripper with adjustable stiffness joints for multiple grasp modes. *Smart Mater. Struct.* **26**, 055035 (2017).
26. L. J. Wood, J. Rendon, R. J. Malak, D. Hartl, An origami-inspired, SMA actuated lifting structure, *Proceedings of the ASME 2016 International Design Engineering Technical Conferences and Computers and Information in Engineering Conference*, Charlotte, NC, 21 to 24 August 2016 (ASME, 2016).
27. J. Kim, D.-Y. Lee, S.-R. Kim, K.-J. Cho, A self deployable origami structure with locking mechanism induced by buckling effect, *Proceedings of the 2015 IEEE International Conference on Robotics and Automation (ICRA)*, Seattle, WA, 26 to 30 May 2015 (IEEE, 2015).
28. J. Ou, L. Yao, J. Steimle, R. Niiyama, H. Ishii, JamSheets: Thin interfaces with tunable stiffness enabled by layer jamming, *Proceedings of the 8th International Conference on Tangible, Embedded and Embodied Interaction*, Munich, Germany, 16 to 19 February 2014 (ACM, 2014).
29. Y.-J. Kim, S. Cheng, S. Kim, K. Iagnemma, A novel layer jamming mechanism with tunable stiffness capability for minimally invasive surgery. *IEEE Trans. Robot.* **29**, 1031–1042 (2013).
30. E. A. Peraza-Hernandez, D. J. Hartl, R. J. Malak Jr., D. C. Lagoudas, Origami-inspired active structures: A synthesis and review. *Smart Mater. Struct.* **23**, 094001 (2014).
31. J. K. Paik, R. J. Wood, A bidirectional shape memory alloy folding actuator. *Smart Mater. Struct.* **21**, 065013 (2012).
32. E. Hawkes, B. An, N. M. Benbernou, H. Tanaka, S. Kim, E. D. Demaine, D. Rus, R. J. Wood, Programmable matter by folding. *Proc. Natl. Acad. Sci. U.S.A.* **107**, 12441–12445 (2010).
33. J.-S. Koh, S.-R. Kim, K.-J. Cho, Self-folding origami using torsion shape memory alloy wire actuators, *Proceedings of the ASME 2014 International Design Engineering Technical Conferences and Computers and Information in Engineering Conference*, Buffalo, NY, 17 to 20 August 2014 (ASME, 2014).
34. M. T. Tolley, S. M. Felton, S. Miyashita, D. Aukes, D. Rus, R. J. Wood, Self-folding origami: Shape memory composites activated by uniform heating. *Smart Mater. Struct.* **23**, 094006 (2014).
35. Y. Liu, B. Shaw, M. D. Dickey, J. Genzer, Sequential self-folding of polymer sheets. *Sci. Adv.* **3**, e1602417 (2017).
36. T. A. Evans, R. J. Lang, S. P. Magleby, L. L. Howell, Rigidly foldable origami gadgets and tessellations. *R. Soc. Open Sci.* **2**, 150067 (2015).
37. T. Tachi, One-DOF cylindrical deployable structures with rigid quadrilateral panels, *Proceedings of the International Association for Shell and Spatial Structures (IASS) Symposium*, Valencia, Spain, 29 September to 2 October 2009 (Editorial Universitat Politècnica de València, 2009).
38. T. Tachi, K. Miura, Rigid-foldable cylinders and cells. *J. Int. Assoc. Shell Spat. Struct.* **53**, 217–226 (2012).
39. G.-P. Jung, J.-S. Koh, K.-J. Cho, Underactuated adaptive gripper using flexural buckling. *IEEE Trans. Robot.* **29**, 1396–1407 (2013).
40. M. Kaneko, T. Yamashita, K. Tanie, Basic considerations on transmission characteristics for tendon drive robots, *Proceedings of the Fifth International Conference on Advanced Robotics, 1991. 'Robots in Unstructured Environments'*, 91 ICAR, Pisa, Italy, 19 to 22 June 1991 (IEEE, 1991).

Acknowledgments: We thank J. J.-R. Song for working on graphical presentation of figures. **Funding:** This material is based on work supported by the National Research Foundation of Korea (NRF) (NRF-2016R1A5A1938472), Institute for Information and Communications Technology Promotion (IITP) (R0190-15-2040), and the Air Force Office of Scientific Research (FA2386-16-1-4052). **Author contributions:** S.-J.K. designed and built the foldable arm, designed and performed experiments, analyzed data, and wrote the manuscript. D.-Y.L. assisted in developing the arm, analyzing data, and organizing the manuscript. G.-P.J. assisted in designing the gripper and writing the manuscript. K.-J.C. directed the project and edited the manuscript. **Competing interests:** K.-J.C., S.-J.K., and D.-Y.L. are inventors on patent application (Kor. 10-2018-0027654) submitted by Seoul National University that covers the structure design of the origami inspired robotic arm. The other authors declare that they have no competing interests. **Data and materials availability:** K.-J.C. may be contacted for additional information.

Submitted 23 October 2017

Accepted 16 February 2018

Published 14 March 2018

10.1126/scirobotics.aar2915

Citation: S.-J. Kim, D.-Y. Lee, G.-P. Jung, K.-J. Cho, An origami-inspired, self-locking robotic arm that can be folded flat. *Sci. Robot.* **3**, eaar2915 (2018).

An origami-inspired, self-locking robotic arm that can be folded flat

Suk-Jun Kim, Dae-Young Lee, Gwang-Pil Jung and Kyu-Jin Cho

Sci. Robotics **3**, eaar2915.
DOI: 10.1126/scirobotics.aar2915

ARTICLE TOOLS

<http://robotics.sciencemag.org/content/3/16/eaar2915>

SUPPLEMENTARY MATERIALS

<http://robotics.sciencemag.org/content/suppl/2018/03/09/3.16.eaar2915.DC1>

REFERENCES

This article cites 30 articles, 5 of which you can access for free
<http://robotics.sciencemag.org/content/3/16/eaar2915#BIBL>

PERMISSIONS

<http://www.sciencemag.org/help/reprints-and-permissions>

Use of this article is subject to the [Terms of Service](#)